Geophys. J. Int. (2006) **166,** 293–308 doi: 10.1111/j.1365-246X.2006.02976.x

Velocity shift in two-dimensional anisotropic random media using the Rytov method

Tatsuhiko Saito

National Research Institute for Advanced Industrial Science and Technology, Central #7, 1-1-1, *Tsukuba, Ibaraki,* 305-8567, *Japan.*
E-mail: tatsu-saito@aist.go.jp

Accepted 2006 February 28. Received 2006 February 26; in original form 2005 November 15

SUMMARY

When high-frequency waves propagate through a randomly inhomogeneous medium, the apparent wave velocity is larger than the spatial average of the velocity distribution. The difference between the two velocities is referred to as the velocity shift. The present study formulates the velocity shift in 2-D anisotropic random media using the Rytov method. Anisotropic random media in (x, z) coordinates are characterized by autocorrelation functions (ACFs) with a long correlation distance along the x-axis and a short correlation distance along the z-axis, where the velocity structure varies smoothly along the x-axis and rapidly along the z-axis. Note that the spatial average values of the velocity distribution along the x-axis and the z-axis are the same. The formulation gives the velocity shift for general types of ACF. An analytic solution is obtained for the case of a Gaussian ACF. To examine the reliability of the Rytov method, the velocity shift is estimated from numerical simulations of wave propagation using Ricker wavelets with dominant frequencies 80 and 40 Hz. The random media are realized with a spatial average velocity of 2700 m s^{-1} and an exponential ACF with 5 per cent rms fractional velocity fluctuation, a correlation distance of 80 m along the x-axis and 40 m along the z-axis. Numerical simulations show that waves apparently propagate faster with increasing travel distance, frequency and the angle of incidence measured from the z-axis to the global ray direction. For example, in the case of the 80 Hz Ricker wavelet at a distance of 520 m, the values of the velocity shift are about 0.9 and 0.3 per cent along the x-axis and the z-axis, respectively. The Rytov method quantitatively explains these general tendencies except for short travel distances along the x-axis. The discrepancy at short travel distances could be due to the small-angle scattering approximation and the long travel distance approximation employed in the Rytov method. Observations of P-wave velocity anisotropy have usually been interpreted in terms of preferred orientations of cracks and minerals in past studies. However this study indicates that wave scattering due to anisotropic random media can provide an alternative explanation for those observations.

Key words: anisotropy, random media, scattering, seismic waves, velocity shift.

1 INTRODUCTION

High-frequency seismograms contain a number of scattered waves in addition to direct P and S waves. Since their detailed features are too complex to be interpreted with simple deterministic structures such as the layered velocity model, seismologists have attempted to simulate the seismograms by assuming random media in which wave velocities fluctuate randomly through space. For example, a coda wave, or the late part of the seismogram, is considered to be composed of scattered waves excited by the small-scale random inhomogeneity (e.g. Aki & Chouet 1975; Fehler & Sato 2003). The early part of the seismogram envelope, which shows an increase in duration and a decrease in amplitude with travel distance, can also be simulated by scattering in the random media (e.g. Sato 1989; Saito *et al.* 2005). Modellings of the seismograms using random media and their applications are well summarized in Sato & Fehler (1998).

In random media, traveltimes observed at stations with the same travel distance differ from station to station. The variance and the covariance of the traveltime fluctuation between the stations reflect properties of the random media. Chernov (1960) derived a theoretical method for calculation of the covariance of the travel time fluctuation in random media. Iooss (1998) extended this method to include anisotropic random media, and Flatté & Wu (1988) extended it with depth dependent structures for application to observed seismological data. It is noteworthy that Aki (1973) first applied Chernov's theory to observed seismograms to estimate subsurface inhomogeneity;

he analysed the correlation between travel time fluctuation and amplitude fluctuation. Kravtsov *et al.* (2003) studied the covariance of reflected wave traveltimes in order to characterize the inhomogeneity above the reflector. Laboratory experimental studies also show that the variance of the traveltime fluctuation depends on the characteristic scale of the inhomogeneity (e.g. Sivaji *et al.* 2001, 2002). Spetzler *et al.* (2002) discussed this phenomenon based on stochastic approaches using scattering theory and ray theory.

Considering that waves propagate preferentially through high-velocity portions in the random media, it follows that the velocity obtained from the average traveltime is greater than the spatial average of the velocity distribution. The difference between the two velocities is referred to as the velocity shift, and it has been investigated using various theoretical approaches. For example, Soviet authors had investigated the velocity shift based on the ray theory at least since 1983; these studies are summarized in Petersen (1990). Wielandt (1987) supposed a spherical velocity anomaly in homogeneous medium and used analytic solutions of the waveforms to investigate the bias of the apparent velocity caused by the spherical anomaly. The most rigorous approach for the velocity shift in random media is to solve the wave equation numerically using the finite-difference (FD) method. The results show that the velocity shift depends on the frequency; high-frequency waves propagate faster than low-frequency waves in random media (e.g. Müller *et al.* 1992; Mukerji *et al.* 1995). This dependence on frequency is one of the candidates for interpreting the discrepancy between velocity structures determined by high-frequency seismograms and those obtained from low-frequency seismograms (Roth *et al.* 1993; Baig & Dahlen 2004). Numerical simulations produce the most reliable value for estimating the velocity shift, but are computationally expensive. On the other hand, high-frequency limit theories, such as those which employ eikonal equation and ray equation, are frequently used to calculate traveltimes due to their usability (e.g. Roth *et al.* 1993; Müller *et al.* 1992). Using the eikonal equation or the ray equation, Avendonk & Snieder (1994) and Samuelides & Mukerji (1998) theoretically derived velocity anisotropy caused by anisotropic random media. Traveltimes calculated using methods based on these equations are frequency independent and usually smaller than those obtained from wave propagation simulations (e.g. Roth *et al.* 1993; Mukerji *et al.* 1995). That is because those equations do not take finite wave frequency effect, or wave scattering, into consideration. These methods work properly when the wave scattering is very weak or the scale of the inhomogeneity is much larger than the wavelength. However, the methods seem to be inappropriate in situations where we have random media with small-scale inhomogeneity.

Small-angle scattering approximation is known to be a good approximation for calculating the early part of seismograms. Some studies have used this approximation for the synthesis of the early part of seismogram envelopes (e.g. Fehler *et al.* 2000; Saito *et al.* 2002; Korn & Sato 2005). Using the small-angle scattering approximation with the Rytov method, Shapiro *et al.* (1996) theoretically derived the velocity shift in isotropic random media. The method successfully explains the frequency dependent velocity shift because it takes wave scattering into consideration. However, because their formulation was limited to isotropic random media, it is not realistic enough to model subsurface inhomogeneity. Anisotropic random media for which the characteristic scale lengths of the inhomogeneity in the vertical and the horizontal directions are different are more appropriate (e.g. Wu *et al.* 1994). It should be noted that this study uses the term 'anisotropic random media', whereas some papers use the term 'anisomeric media' to distinguish anisotropy of the elastic tensor (e.g. Kravtsov *et al.* 2003). Note that this study does not consider anisotropy of the elastic tensor. Samuelides (1998) derived the velocity shift in anisotropic random media with the Rytov method, for the special case of random media characterized by a Gaussian autocorrelation function (ACF). It is necessary to extend this approach to the velocity shift in anisotropic random media characterized by a general ACF. Also, the relation between Shapiro *et al.* (1996) and Samuelides (1998) is unclear; their formulations, which are different, give different resultant equations even though both approaches employ the Rytov method.

The main purpose of this study is to derive the velocity shift in 2-D anisotropic random media using the Rytov method. We also show that the two different approaches, Shapiro *et al.* (1996) and Samuelides (1998), produce the same resultant equations when we make some approximations. In Section 2, we discuss 2-D anisotropic random media. In Section 3, the velocity shift in anisotropic random media is formulated using the Rytov method. This formulation is an extension of Samuelides (1998). Another formulation, which is based on Shapiro *et al.* (1996), is presented in Appendix B. In Section 4, we simulate wave propagation numerically with the FD method to estimate the apparent velocity. To examine the reliability of the Rytov method, we compare the values of velocity shift obtained from the Rytov method with those from the FD method. In Section 5, we discuss some noteworthy properties of the velocity shift. Finally, Section 6 presents some conclusions.

2 2-D ANISOTROPIC RANDOM MEDIA

We suppose the velocity structure is given by $V(\boldsymbol{x}) = V_0\{1 + \xi(\boldsymbol{x})\}$, where the spatial average velocity V_0 is constant and the fractional velocity fluctuation $\xi(\boldsymbol{x})$ is a random function of the spatial coordinates $\boldsymbol{x}$. Throughout this study, a weak fluctuation with $|\xi| \ll 1$ is assumed. To obtain statistical properties of the media, we consider an ensemble of the fractional fluctuation $\{\xi(\boldsymbol{x})\}$ such that $\langle\xi(\boldsymbol{x})\rangle = 0$, where the angular brackets denote the ensemble average. When the random media are statistically homogeneous in space, the media are characterized by an ACF, $R(\boldsymbol{x}_d) \equiv \langle\xi(\boldsymbol{x}_d + \boldsymbol{x})\xi(\boldsymbol{x})\rangle$, which depends on the difference vector $\boldsymbol{x}_d$ but not on the location $\boldsymbol{x}$. In 2-D random media, the ACF is generally described using the rms value of the fractional velocity fluctuation ε and two correlation distances a_x and a_z, which are the characteristic scale lengths of the inhomogeneity in the x and z directions, respectively. In the (x, z) coordinates, the ACF of the anisotropic random media is represented by

$$R_{xz}(x_d, z_d) = \varepsilon^2 \bar{R}\left(\sqrt{\frac{{x_d}^2}{{a_x}^2} + \frac{{z_d}^2}{{a_z}^2}}\right) = \varepsilon^2 \bar{R}(\bar{r}), \tag{1}$$

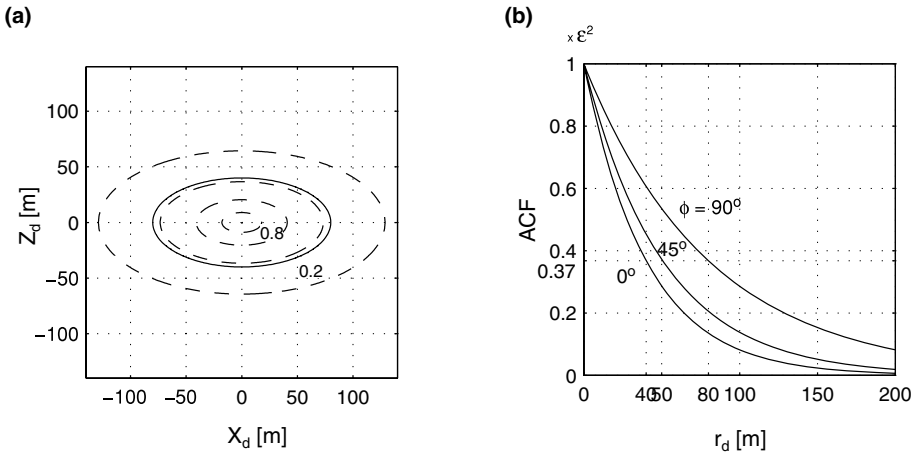

Figure 1. (a) Contour plot of the von Kármán-type ACF with $\kappa = 0.5$, or exponential ACF. The two correlation distances are $a_x = 80$ m, $a_z = 40$ m along the x-axis and the z-axis, respectively. The values normalized by mean-square fractional velocity fluctuation ε^2 are plotted on dashed curves with a step of 0.2. Also, the value e^{-1} is plotted by a solid curve. (b) Cross-sections of the ACF for different directions are plotted for $\phi = 0$, $\pi/4$, and $\pi/2$, where ϕ is measured from the z_d-axis.

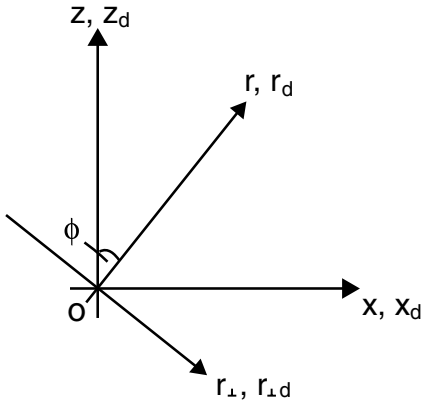

Figure 2. Coordinates used in the formulation of 2-D anisotropic media (x-z space). The global ray direction from a source is in the radial direction r. A transverse axis $r_\perp$ is orthogonal to the axis r. The angle of incidence ϕ is the angle between the z-axis and the r-axis. Coordinates $(r_{\perp d}, r_d)$ represent the difference between two points $(r_{\perp 1}, r_1)$ and $(r_{\perp d}, r_1)$. The values of $r_{\perp d}$ and r_d are defined by $r_{\perp d} \equiv r_{\perp 1} - r_{\perp 2}$ and $r_d \equiv r_1 - r_2$, respectively.

where x_d and z_d are the spatial lags in the x and z directions, $\bar{R}(\bar{r})$ is the normalized ACF, $\bar{r}$ is the normalized difference distance defined by

$$\bar{r} \equiv \sqrt{\frac{{x_d}^2}{{a_x}^2} + \frac{{z_d}^2}{{a_z}^2}}. \tag{2}$$

The normalized ACFs of the Gaussian and von Kármán type are given by

$$\bar{R}(\bar{r}) = \begin{cases} \exp\left(-\bar{r}^2\right) & \text{Gaussian.} \\ \dfrac{2^{1-\kappa}}{\Gamma(\kappa)} \bar{r}^{\kappa} K_\kappa(\bar{r}) \quad \kappa > 0 & \text{vonKarman.} \end{cases} \tag{3}$$

The von Kármán type ACF coincides exactly with the exponential ACF when $\kappa = 0.5$. For example, Fig. 1(a) shows the exponential ACF characterized by the correlation distances, $a_x > a_z$.

We introduce coordinates $(r_\perp, r)$ rotated by a clockwise angle ϕ from the coordinates (x, z) (Fig. 2). The r-axis will be taken as the global ray direction in the formulation. A difference vector $(r_d, r_{\perp d})$ can also be defined in the $(r_\perp, r)$ coordinates. The relation between (x_d, z_d) and $(r_{\perp d}, r_d)$ is given by

$$x_d = r_{\perp d} \cos\phi + r_d \sin\phi \quad \text{and} \quad z_d = -r_{\perp d} \sin\phi + r_d \cos\phi. \tag{4}$$

In $(r_\perp, r)$ coordinates, the ACF is expressed as

$$R(r_{\perp d}, r_d) = R_{xz}(r_{\perp d} \cos\phi + r_d \sin\phi, -r_{\perp d} \sin\phi + r_d \cos\phi). \tag{5}$$

The cross-section of the ACF along the r_d-axis is

$$R(0, r_d) = R_{xz}(r_d \sin\phi, r_d \cos\phi) = \varepsilon^2 \bar{R}\left(\frac{r_d}{a_r}\right), \tag{6}$$

where a_r is defined by

$$a_r \equiv a_x a_z / \sqrt{a_x{}^2 \cos^2\phi + a_z{}^2 \sin^2\phi}, \tag{7}$$

and can be considered as a correlation distance along the r-axis. Fig. 1(b) shows the ACF along the r_d-axis for $\phi = 0, \pi/4$ and $\pi/2$.

The power spectral density function (PSDF) of the fractional velocity fluctuation also characterizes the random media. The PSDF in the (x, z) coordinates is given in terms of the ACF as

$$\begin{aligned} P_{xz}(m_x, m_z) &= \int_{-\infty}^{\infty}\int_{-\infty}^{\infty} R_{xz}(x_d, z_d)\exp(-im_x x_d - im_z z_d)\,dx_d\,dz_d \\ &= 2\pi\varepsilon^2 a_x a_z \int_0^{\infty} J_0(\bar{m}\bar{r})\bar{r}\,\bar{R}\,(\bar{r})\;d\bar{r} \\ &= \varepsilon^2 a_x a_z \bar{P}(\bar{m}), \end{aligned} \tag{8}$$

where the normalized PSDF is defined by

$$\bar{P}(\bar{m}) \equiv 2\pi \int_0^{\infty} J_0(\bar{m}\bar{r})\bar{r}\,\bar{R}(\bar{r})\,d\bar{r}, \tag{9}$$

and the normalized wavenumber is given by

$$\bar{m} \equiv \sqrt{a_x{}^2 m_x{}^2 + a_z{}^2 m_z{}^2}. \tag{10}$$

The normalized PSDFs for the Gaussian and von Kármán-type are given by

$$\bar{P}(\bar{m}) = \begin{cases} \pi\exp(-\bar{m}^2/4) & \text{Gaussian.} \\ \dfrac{4\pi\kappa}{(1+\bar{m}^2)^{\kappa+1}}, \quad \kappa > 0 & \text{von Karman..} \end{cases} \tag{11}$$

The PSDF in the $(r_\perp, r)$ coordinates and the corresponding ACF are given by

$$\begin{aligned} P(m_\perp, m_r) &= \int_{-\infty}^{\infty}\int_{-\infty}^{\infty} R(r_{\perp d}, r_d)\exp\left(-im_\perp r_{\perp d} - im_r r_d\right)dr_{\perp d}dr_d \\ &= P_{xz}(m_\perp\cos\phi + m_r\sin\phi, -m_\perp\sin\phi + m_r\cos\phi) \\ &= \varepsilon^2 a_x a_z \bar{P}\left(\sqrt{a_x^2(m_\perp\cos\phi + m_r\sin\phi)^2 + a_z^2(-m_\perp\sin\phi + m_r\cos\phi)^2}\right), \end{aligned} \tag{12}$$

and

$$\begin{aligned} R\,(r_{\perp d}, r_d) &= \frac{1}{(2\pi)^2}\int_{-\infty}^{\infty}\int_{-\infty}^{\infty} P\,(m_\perp, m_r)\exp\left(im_\perp r_{\perp d} + im_r r_d\right)\,dm_\perp dm_r \\ &= \frac{\varepsilon^2 a_x a_z}{(2\pi)^2}\int_{-\infty}^{\infty}\int_{-\infty}^{\infty}\exp\left(im_\perp r_{\perp d} + im_r r_d\right)dm_\perp dm_r \\ &\quad\times\bar{P}\left(\sqrt{a_x^2(m_\perp\cos\phi + m_r\sin\phi)^2 + a_z^2(-m_\perp\sin\phi + m_r\cos\phi)^2}\right), \end{aligned} \tag{13}$$

respectively.

3 VELOCITY SHIFT WITH THE RYTOV METHOD

3.1 Velocity shift

Let us consider propagation of a scalar wave $u(\boldsymbol{x}, t)$ through 2-D random media governed by

$$\left(\Delta - \frac{1}{V\,(\boldsymbol{x})^2}\frac{\partial^2}{\partial t^2}\right)u(\boldsymbol{x}, t) = 0, \tag{14}$$

where $\boldsymbol{x} = (x, z)$ and Δ is the Laplacian in 2-D. The velocity structure is given by $V(\boldsymbol{x}) = V_0\{1 + \xi(\boldsymbol{x})\}$. We suppose a plane wave incident to the random media as shown in Fig. 3. When we consider a monochromatic wave $u(\boldsymbol{x}, t) = \hat{u}(\boldsymbol{x})\exp(-i\omega t)$ with angular frequency ω in weak random media i.e. with $|\xi| \ll 1$, we can rewrite the wave equation as

$$\Delta\hat{u}(\boldsymbol{x}) + k^2\hat{u}(\boldsymbol{x}) = 2\,\xi(\boldsymbol{x})k^2\hat{u}(\boldsymbol{x}), \tag{15}$$

where the wavenumber $k = \omega/V_0$. Coordinates $(r_\perp, r)$ are used; the r-axis is in the global ray direction and the $r_\perp$-axis is perpendicular to the r-axis. The random inhomogeneity is distributed in the region $r > 0$, while the velocity is homogeneous in the region $r < 0$. Setting

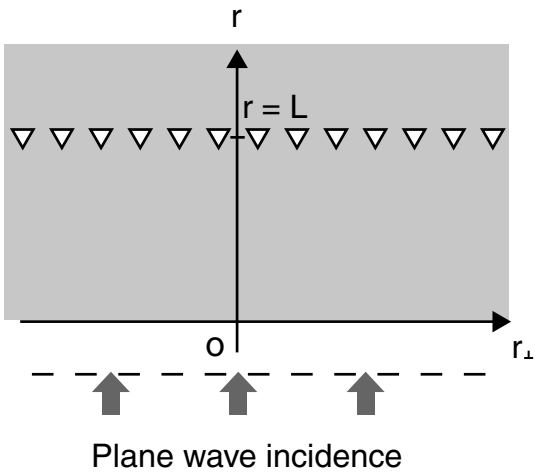

Figure 3. Geometry of plane wave incident into the inhomogeneous zone ($r > 0$). Stations constituting a line array located at a travel distance L observe the wavefield.

$\hat{u}(\boldsymbol{x}) = U(r_\perp, r)\exp(ikr)$ in eq. (15) and neglecting the second derivative with respect to r, we obtain

$$2ik\frac{\partial U(r_\perp, r)}{\partial r} + \frac{\partial^2 U(r_\perp, r)}{\partial {r_\perp}^2} - 2\xi(r_\perp, r)k^2 U(r_\perp, r) = 0. \tag{16}$$

The equation is known as the parabolic equation. It focuses on the small-angle scattering of waves and is valid when the large-angle is negligibly small (e.g. Rytov *et al.* 1989; Sato & Fehler 1998). Small-angle scattering dominates large-angle scattering when ka_x, $ka_z \gg 1$ (e.g. p.92 Sato & Fehler 1998). Wavetraces are observed at an array of stations in a line with a travel distance L (Fig. 3). Even though all the stations are located at the same travel distance, traveltimes differ between stations due to the velocity fluctuation. With reference to Shapiro *et al.* (1996), the traveltime of a given phase at a location ($r_\perp$, L) is represented as

$$t(r_{\perp i}, L) = \frac{\text{phase}}{\omega} = \frac{\varphi_0(L) + \varphi(r_{\perp i}, L)}{\omega}, \tag{17}$$

where the phase is decomposed into the phase $\varphi_0(L) = kL$ in homogeneous media with velocity V_0 and its phase fluctuation $\varphi(r_{\perp i}, L)$. We set the phase equal to zero at travel distance $L = 0$. For a long line array with a sufficiently large number of stations, the average traveltime over the stations is supposed to be the same as the ensemble average of the traveltimes $\langle t(r_{\perp i}, L)\rangle$ with respect to the ensemble of random media. We note that spatial ergodicity is assumed here. This study defines the effective average velocity and the velocity shift as $V_{\text{eff}} \equiv L/\langle t(r_{\perp i}, L)\rangle$ and $\delta V/V \equiv (V_{\text{eff}} - V_0)/V_0$, respectively. The velocity shift is approximated as

$$\frac{\delta V}{V_0} \approx -\frac{\langle t(r_{\perp i}, L)\rangle - T_0}{T_0} = -\frac{\langle\varphi\rangle}{kL} \quad \text{when} \quad \left|\frac{\langle\varphi\rangle}{kL}\right| \ll 1, \tag{18}$$

where the traveltime is given by $T_0 \equiv L/V_0$ in the homogeneous medium $V(\boldsymbol{x}) = V_0$. We estimate the ensemble average phase-fluctuation $\langle\varphi\rangle$ with the Rytov method in the next subsection.

3.2 The Rytov method

With reference to the method of Samuelides (1998), we formulate the velocity shift in 2-D anisotropic random media based on the Rytov method. When a plane wave with unit amplitude propagates into the random media, the wavefield $U(r_\perp, r)$ is represented with a complex value $\Xi(r_\perp, r)$ as

$$U(r_\perp, r) = \exp\{\Xi(r_\perp, r)\} = \exp\{\mathrm{Re}\Xi(r_\perp, r) + i\,\mathrm{Im}\Xi(r_\perp, r)\}, \tag{19}$$

where the real part $\mathrm{Re}\Xi$ denotes the log-amplitude fluctuation and the imaginary part $\mathrm{Im}\Xi$ denotes the phase fluctuation, $\mathrm{Im}\Xi = \varphi$. A perturbation method for the wavefield calculation with this transformation (19) is known as the Rytov method (e.g. Ishimaru 1978; Rytov *et al.* 1989; Sato & Fehler 1998). We suppose that the wavefield fluctuation is weak and the wavefield $\Xi(r_\perp, r)$ can be expressed as a power series with respect to the rms value of the fractional velocity fluctuation,

$$\Xi(r_\perp, r) = \varepsilon\Xi_1(r_\perp, r) + \varepsilon^2\Xi_2(r_\perp, r) + O(\varepsilon^3). \tag{20}$$

Substituting eqs (19) and (20) into eq. (16) and keeping terms up to the second order gives

$$2ik\frac{\partial\Xi_1(r_\perp, r)}{\partial r} + \frac{\partial^2\Xi_1(r_\perp, r)}{\partial {r_\perp}^2} - 2k^2\frac{\xi(r_\perp, r)}{\varepsilon} = 0, \tag{21}$$

$$2ik\frac{\partial\Xi_2(r_\perp, r)}{\partial r} + \frac{\partial^2\Xi_2(r_\perp, r)}{\partial {r_\perp}^2} + \left(\frac{\partial\Xi_1(r_\perp, r)}{\partial r_\perp}\right)^2 = 0, \tag{22}$$

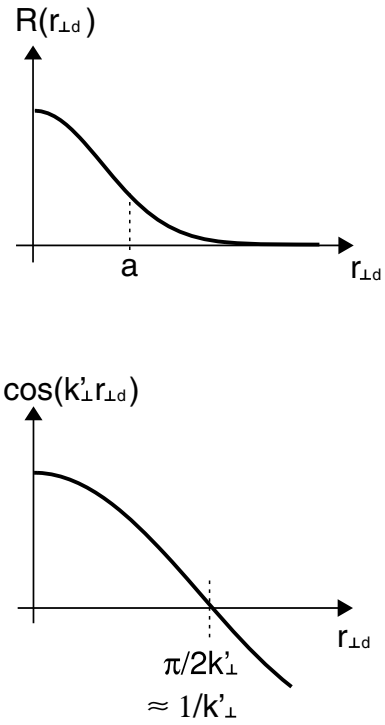

Figure 4. Decay of ACF $R(r_{\perp d})$ and cos $(k'_{\perp}\, r_{\perp d})$ against $r_{\perp d}$.

where we should note that $\xi = O(\varepsilon)$. By using the Fourier transform with respect to $r_{\perp}$, we obtain a solution of eq. (21),

$$\Xi_1(r_\perp, r) = -\frac{ik}{2\varepsilon\pi}\int_0^r dr' \int_{-\infty}^{\infty} dk_\perp \exp\left\{ik_\perp r_\perp - i\frac{{k_\perp}^2 (r-r')}{2k}\right\}\hat{\xi}(k_\perp, r'), \tag{23}$$

where

$$\hat{\xi}(k_\perp, r) = \int_{-\infty}^{\infty} \xi(r_\perp, r)\exp(-ik_\perp r_\perp)\, dr_\perp. \tag{24}$$

Taking the ensemble average of eq. (23), we obtain $\langle \Xi_1 \rangle = 0$. Substituting eq. (23) into eq. (22), we can solve eq. (22). Taking the ensemble average of the solution, we obtain

$$\langle \Xi_2(r_\perp, L)\rangle = -\frac{ik}{4\pi\varepsilon^2}\int_0^L dr \int_0^r dr' \int_0^r dr'' \int_{-\infty}^{\infty} dk'_\perp {k'_\perp}^2 \exp\left\{-\frac{ik'^2_\perp (2r - r' - r'')}{2k}\right\}$$
$$\times \int_{-\infty}^{\infty} dr_{\perp d}\, R(r_{\perp d}, r' - r'')\exp\left(-ik'_\perp r_{\perp d}\right). \tag{25}$$

This equation corresponds to eq. (17) in Samuelides (1998). A more detailed derivation is presented in Appendix A. Introducing centre of mass and difference coordinates with respect to r' and r'', $r_c = (r' + r'')/2$ and $r_d = r' - r''$, and calculating the imaginary part of the solution (25), we obtain

$$\mathrm{Im}\langle \Xi_2(r_\perp, L)\rangle = -\frac{k^2}{2\pi\varepsilon^2}\int_0^L dr \int_{-r}^{r} dr_d \int_{-\infty}^{\infty} dk'_\perp \int_{-\infty}^{\infty} dr_{\perp d}$$
$$\cos(k'_\perp r_{\perp d})\cos\left(\frac{{k_\perp}^2 r}{2k}\right)\sin\left\{\frac{{k'_\perp}^2 (r - |r_d|)}{2k}\right\} R(r_{\perp d}, r_d). \tag{26}$$

When we consider the variation of correlation function $R(r_{\perp d}, r_d)$ and the factor cos $(k'_\perp r_{\perp d})$ in the integrand of eq. (26) with respect to $r_{\perp d}$ (see Fig. 4), we observe that the contribution of the integrand is dominant when $1/k'_\perp \approx a$ or $1/k'_\perp > a$, where a is the larger of a_x and a_z. We use the abbreviation $k'_\perp \lesssim 1/a$ to represent the condition $k'_\perp \approx 1/a$ or $k'_\perp < 1/a$, hereinafter. Also, we note that $R(r_{\perp d}, r_d)$ is small when $r_{\perp d} > a$. Using these relations and the condition $ak \gg 1$ used in the derivation of the parabolic wave equation, we obtain the following inequalities,

$$\frac{{k'_\perp}^2 |r_d|}{2k} \lesssim \frac{{k'_\perp}^2 a}{2k} \lesssim \frac{1}{2ak} \ll 1, \tag{27}$$

with the result that

$$\cos\left(\frac{{k'_\perp}^2 |r_d|}{2k}\right) \approx 1 \quad \text{and} \quad \sin\left(\frac{{k'_\perp}^2 |r_d|}{2k}\right) \approx 0. \tag{28}$$

Using eqs (28) and (26) can be approximated as

$$\begin{aligned}\mathrm{Im}\langle \Xi_2(r_\perp, L)\rangle &\approx -\frac{k^2}{4\pi\varepsilon^2}\int_0^L dr\int_{-r}^{r} dr_d\int_{-\infty}^{\infty} dk'_\perp\int_{-\infty}^{\infty} dr_{\perp d}\cos(k'_\perp r_{\perp d})\sin\left\{\frac{{k'_\perp}^2 r}{k}\right\}R(r_{\perp d}, r_d)\\ &\approx -\frac{k^2}{4\pi\varepsilon^2}\int_0^L dr\int_{-\infty}^{\infty} dr_d\int_{-\infty}^{\infty} dk'_\perp\int_{-\infty}^{\infty} dr_{\perp d}\cos(k'_\perp r_{\perp d})\sin\left\{\frac{{k'_\perp}^2 r}{k}\right\}R(r_{\perp d}, r_d).\end{aligned} \tag{29}$$

In eq. (29), we also used the condition $L \gg a_r$ to change the integration range of r_d where a_r is defined by eq. (7). Substituting eq. (13) into eq. (29) and integrating with respect to r_d, m_r, $r_{\perp d}$, $m_\perp$ and r in turn, we obtain

$$\mathrm{Im}\langle \Xi_2(r_\perp, L)\rangle \approx -\frac{k^3}{\pi\varepsilon^2}\int_0^\infty dk'_\perp\frac{1}{{k'_\perp}^2}\sin^2\left\{\frac{{k'_\perp}^2 L}{2k}\right\}P(k'_\perp, 0). \tag{30}$$

Finally, using eqs (18) and (30), we obtain the velocity shift as

$$\begin{aligned}\frac{\delta V}{V_0} &\approx -\frac{\langle\varphi\rangle}{kL} = -\frac{\langle \mathrm{Im}\,\Xi\rangle}{kL} \approx -\frac{\varepsilon^2\mathrm{Im}\langle\Xi_2\rangle}{kL}\\ &= \frac{k^2}{\pi L}\int_0^\infty dk_\perp\frac{1}{{k_\perp}^2}\sin^2\left\{\frac{{k_\perp}^2 L}{2k}\right\}P(k_\perp, 0)\\ &= \frac{\varepsilon^2 k^2 a_t a_r}{\pi L}\int_0^\infty dk_\perp\frac{1}{{k_\perp}^2}\sin^2\left\{\frac{{k_\perp}^2 L}{2k}\right\}\bar{P}(a_t k_\perp),\end{aligned} \tag{31}$$

where the effective correlation distances are defined by

$$a_t \equiv \sqrt{{a_x}^2\cos^2\phi + {a_z}^2\sin^2\phi} \ \text{ and } \ a_r \equiv a_x a_z\Big/\sqrt{{a_x}^2\cos^2\phi + {a_z}^2\sin^2\phi}. \tag{32}$$

The angle ϕ measured from the z-axis to the r-axis is referred to as incident angle, hereinafter. These correlation distances are the same as those obtained by Saito (2005). The velocity shift given by eq. (31) can also be obtained with another method based on Shapiro *et al.* (1996) (see Appendix B). It should be noted that eq. (30) corresponds to the second term of eq. (24) in Shapiro *et al.* (1996), and that the third term of eq. (24) in Shapiro *et al.* (1996) is negligibly small when $ka_x, ka_z \gg 1$. By integration in eq. (31), we can calculate the velocity shift in the random media characterized by a general expression of the PSDF.

For the special case of the random media characterized by a Gaussian PSDF, we obtain eq. (31) in analytical form as

$$\begin{aligned}\frac{\delta V}{V_0} &= \frac{\sqrt{\pi}\varepsilon^2(ka_t)(ka_r)}{2\sqrt{kL}}\\ &\quad\times\left[\left(1+\frac{(ka_t)^4}{16(kL)^2}\right)^{1/4}\cos\left(\frac{1}{2}\arcsin\left\{\left(1+\frac{(ka_t)^4}{16(kL)^2}\right)^{-1/2}\right\}\right)-\left(\frac{(ka_t)^2}{4kL}\right)^{1/2}\right].\end{aligned} \tag{33}$$

This equation is the same as eq. (34) in Shapiro *et al.* (1996) except for the use of the effective correlation distances, a_t and a_r. In the high-frequency limit, $ka_t \gg L/a_t$, so for the velocity shift in the Gaussian PSDF case, eq. (31) yields

$$\begin{aligned}\frac{\delta V}{V_0} &= \frac{\varepsilon^2 k^2 a_\perp a_r}{\pi L}\int_0^\infty\frac{1}{{k_\perp}^2}\sin^2\left(\frac{{k_\perp}^2 L}{2k}\right)\pi\exp\left\{-\frac{{a_\perp}^2{k_\perp}^2}{4}\right\}dk_\perp\\ &\approx \frac{\varepsilon^2 a_\perp a_r L}{4}\int_0^\infty {k_\perp}^2\exp\left\{-\frac{{a_\perp}^2{k_\perp}^2}{4}\right\}dk_\perp\\ &= \frac{\sqrt{\pi}\varepsilon^2 a_r L}{2{a_\perp}^2}.\end{aligned} \tag{34}$$

3.3 Weak wavefield fluctuation

In the Rytov method, we assumed that the wavefield fluctuation is weak (eq. 20). In order to measure how large the wavefield fluctuation is, ensemble average wavefield, or coherent wavefield $\langle U(r_\perp, r)\rangle$ is introduced. When the intensity of $\langle U(r_\perp, r)\rangle$ is much smaller than the total wavefield intensity $\langle|U|^2\rangle$, we consider that the wavefield fluctuation is weak (Shapiro *et al.* 1996). With reference to Sato & Fehler (p. 242, 1998), the coherent wavefield in anisotropic random media is calculated as

$$\langle U(r_\perp, r)\rangle \approx \exp\left\{-\frac{\varepsilon^2(ka_r)^2}{4\pi}\frac{L}{a_r}\int_{-\infty}^{\infty}\bar{P}(\bar{m})\,d\bar{m}\right\} \tag{35}$$

From eq. (35), we find that the value of $\vartheta \equiv \varepsilon^2(ka_r)^2(L/a_r)$ can be a good measure for the attenuation of the coherent wavefield. This value was also used in Shapiro *et al.* (1996) and Samuelides (1998). When the value of ϑ is not too large in comparison with 1, we may consider that the wavefield fluctuation is weak. For example, Shapiro *et al.* (1996) found good agreement between the values of the velocity shift calculated with the Rytov method and calculated with the FD simulations for $\vartheta < 4$ in the case of isotropic random media.

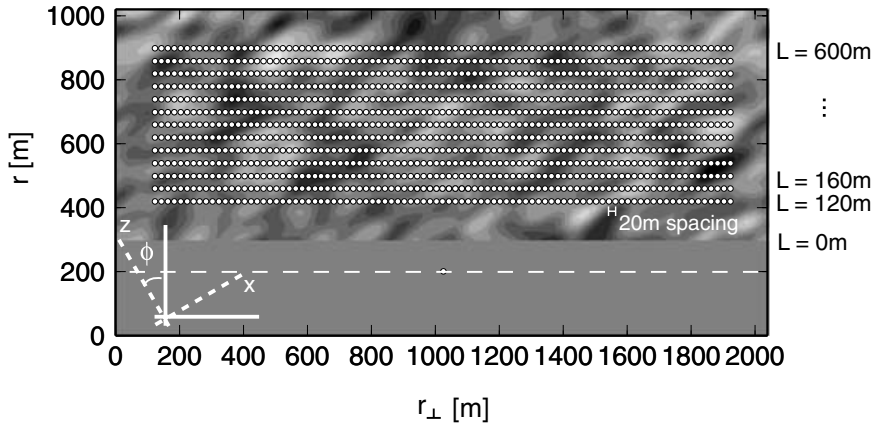

Figure 5. Geometry of finite-difference (FD) simulations. Edges at $r_\perp = 0$ and 2046 m are cyclic boundary conditions. Edges at $r = 0$ and 1022 m are absorbing boundary conditions. The grid spacing is 2 m. The random inhomogeneity occurs for $r > 300$ m. Plane waves excited at $r = 200$ m propagate into the inhomogeneous region. Line arrays are deployed at travel distances L ranging from 120 to 600 with 40 m spacings, where the travel distance L is measured from $r = 300$ m. A line array consists of 91 stations at 20 m intervals. The angle between the z-axis and the r-axis is ϕ.

4 VELOCITY SHIFT WITH NUMERICAL SIMULATIONS

In this section, wave propagation in anisotropic random media is numerically simulated. The velocity shift estimated from the numerical simulation will be compared with the velocity shift calculated by using the Rytov method.

4.1 Wave propagation with finite-difference simulations

Fig. 5 shows the geometry for the numerical calculations in $(r_\perp, r)$ coordinates; the dimensions are 2046 m along the $r_\perp$-axis and 1022 m along the r-axis. The region is discretized with grid spacing 2 m. Absorbing boundaries are applied at $r = 0$ and 1022 m, and periodic boundaries are applied at $r_\perp = 0$ and 2046 m. Random inhomogeneity is assumed for the region defined by $r > 300$ m, while for $r < 300$ m the velocity is homogeneous; $V_0 = 2700$ m s^{-1}. We consider the random inhomogeneity to be characterized by an exponential ACF with $a_x = 80$ m, $a_z = 40$ m and $\varepsilon = 5$ per cent, where the angle between the z-axis and the r-axis is ϕ. We use two source time functions for the Ricker wavelets; one with dominant frequency 80 Hz and the other with dominant frequency 40 Hz. It should be noted that source time functions with a finite frequency band are used to simulate seismic wave propagation although we assumed monochromatic waves in the Rytov method. The formulation assuming monochromatic waves seems to work properly even for the waves with a finite frequency band when the band is not too broad (e.g. Shapiro *et al.* 1996). The dominant wavelengths are about 34 and 68 m for 80 and 40 Hz, respectively; $ka_x \approx 15$ and $ka_z \approx 7$ for 80 Hz and $ka_x \approx 7$ and $ka_z \approx 4$ for 40 Hz. Plane waves, excited at $r = 200$ m, propagate into the inhomogeneous region with the global ray direction along the r-axis. Line arrays are deployed in the inhomogeneous region with travel distances L from 120 to 600 with 40 m spacing; a line array consists of 91 stations placed at 20 m intervals. The orders of the parameters in our simulations are the same as Shapiro *et al.* (1996). The ratio $a_x/a_z = 2$ is consistent with that of KTB borehole data (Wu *et al.* 1994). The range of the measure ϑ (see eq. 35) in our numerical simulations is that $\vartheta \leq 4.2$; when the 80 Hz Ricker wavelets are observed at a distance of 600 m along the x-axis, the value of ϑ reaches the maximum value, $\vartheta = 4.2$. The wave propagations are numerically simulated by the FD method with fourth-order accuracy in space and second-order accuracy in time, with time steps of 0.25 ms. In order to investigate statistical properties of the wavefield, we performed the numerical simulation for 20 realizations of the random media.

Fig. 6 shows examples of wavetraces for the 80 Hz Ricker-wavelet source calculated by the FD method. The three columns correspond to the three propagation directions, $\phi = 0, \pi/4$ and $\pi/2$; the five panels in each column correspond to the five travel distances, 120, 240, 360, 480 and 600 m. The time axes in the panels are reduced with the spatial average velocity $V_0 = 2700$ m s^{-1}. We measure traveltimes of initial waves from these numerically simulated wavetraces. Due to the deformation of waveforms, it is not easy to define the onset, so this study employs two criteria to avoid the bias caused by using a single criterion. As the first criterion, the first significant local minimum, or the first trough, is used for the onset. The traveltime corresponding to this criterion is denoted by t_1. As the second criterion, the zero crossing after the traveltime t_1, is taken as the onset. This traveltime is denoted by t_2. Examples of these criteria in use are shown together with the wave traces in Fig. 6.

We selected traveltimes of wave traces with respect to 20 random media for each propagation direction, $\phi = 0, \pi/4$ and $\pi/2$. The traveltimes at the station located at $(r_{\perp j}, L)$ for the ith medium with propagation direction ϕ are denoted by $t_{1,i}(r_{\perp j}, L, \phi)$ and $t_{2,i}(r_{\perp j}, L, \phi)$ corresponding to the first and second criterion, respectively. According to eq. (18), we estimate the velocity shift from the FD simulations as

$$-\frac{\langle t_{1,j}(r_{\perp j}, L, \phi)\rangle_{i,j} - T_{01}(L)}{T_{01}(L)}, \text{ and } -\frac{\langle t_{2,j}(r_{\perp j}, L, \phi)\rangle_{i,j} - T_{02}(L)}{T_{02}(L)}, \tag{36}$$

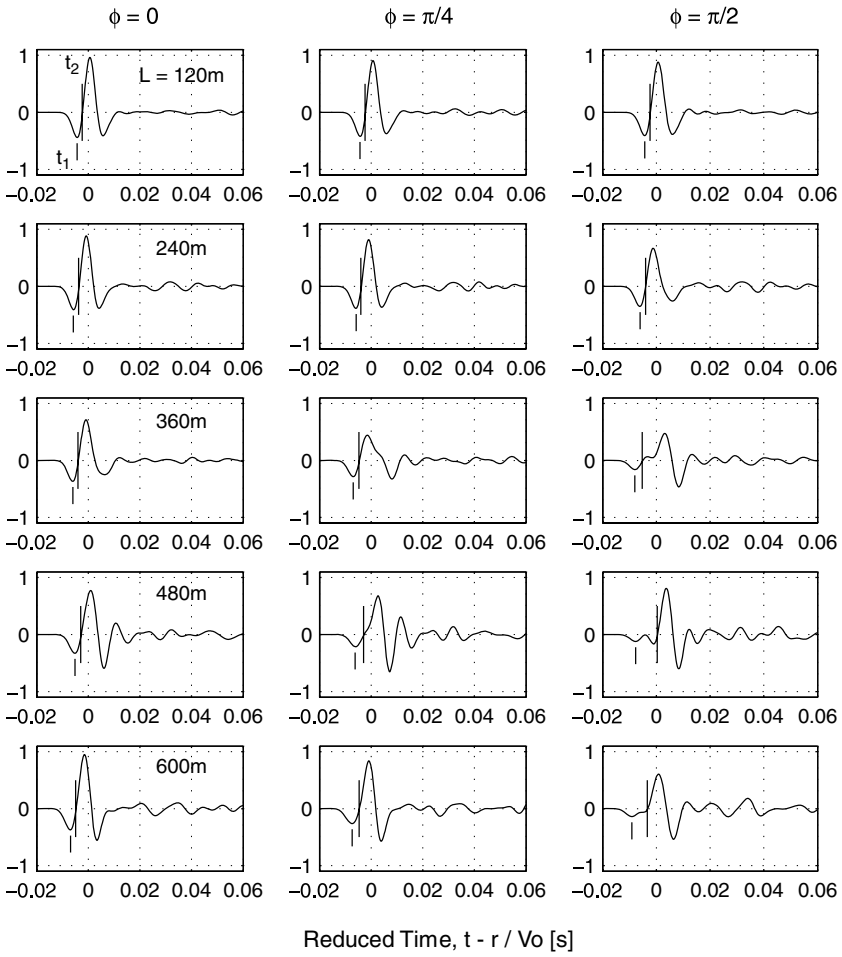

Figure 6. Wave traces calculated by the FD simulations. A Ricker wavelet of dominant frequency 80 Hz propagates through the random media characterized by an exponential ACF with $\varepsilon = 0.05$, $a_x = 80$, $a_z = 40$ m and $V_0 = 2700$ m s^{-1}. A set of five panels in each column is calculated for each angle of incidence ($\phi = 0, \pi/4$ and $\pi/2$). The five panels show the wave traces at stations located at $L = 120$, 240, 360, 480 and 600 m. Time axes are reduced with the spatial average velocity V_0.

for the first and second criterion, respectively. Corresponding traveltimes are denoted by T_{01} and T_{02}, respectively, in the reference medium $V(\boldsymbol{x}) = V_0$; these traveltimes are obtained from the wavetraces of the FD simulations.

4.2 Comparisons: the Rytov method versus FD simulations

It may be useful to show the velocity shift in isotropic random media before considering the case of anisotropic random media. Figs 7(a) and (b) show the velocity shift in isotropic random media of an exponential ACF ($a_x = a_z = 60$ m) for a dominant frequency f_c= 80 Hz and 40 Hz, respectively. The values obtained from the FD simulations are plotted by triangles and circles with error bars; triangles and circles are calculated with t_1 and t_2, respectively. The error bars are estimated with a bootstrap method; we estimate the standard deviation over 25 synthesized values of eq. (36) which are calculated from 25 sets of artificial data. Each artificial data set is generated by 20 random media, which are randomly sampled from the 20 realizations of the random media used in the numerical simulations. The velocity shift increases with increasing travel distance, although this tendency is more prominent in the case of $f_c = 80$ Hz than 40 Hz. Solid curves denote the theoretical predictions obtained from the Rytov method (eq. 31). This theoretically predicted velocity shift matches closely the velocity shift estimated from the FD simulations.

Fig. 8 shows the velocity shift in the anisotropic random media. The three panels on the left are for the dominant frequency f_c = 80 Hz. The velocity shift from the numerical simulations (grey area) increases with increasing travel distance similar to the case of the isotropic random media. Furthermore, the velocity shift becomes larger as the angle of incidence ϕ increases. In other words, the effective average velocity shows anisotropy. The values of the velocity shift calculated from the FD simulations at the travel distance 520 m are about 0.3, 0.5 and 0.9 per cent for the angles of incidence $\phi = 0$, $\pi/4$ and $\pi/2$, respectively. The three panels on the right are for the dominant frequency $f_c = 40$ Hz. The velocity shift from the numerical simulations (grey area) increases with increasing travel distance and angle of

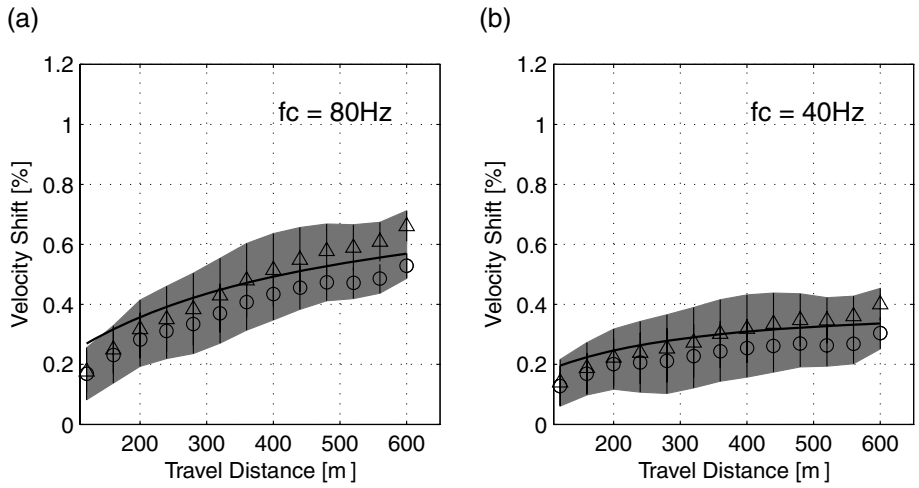

Figure 7. Velocity shift versus travel distance in isotropic random media characterized by an exponential ACF with $\varepsilon = 0.05$, $a_x = 60$, $a_z = 60$ m and $V_0 = 2700$ m s^{-1}. Dominant frequencies are (a) 80 and (b) 40 Hz. Solid curves are plotted with values calculated using the Rytov method and the shaded areas are estimated from FD simulations. Triangles and circles are calculated from the velocity shift with t_1 and t_2 onsets, respectively. Error bars are estimated with a bootstrap method.

incidence as in the case of $f_c = 80$ Hz. The velocity shift of $f_c = 40$ Hz is smaller than that of $f_c = 80$ Hz for comparable travel distances and angles of incidence.

The values of the velocity shift calculated with the Rytov method using eq. (31) are plotted with solid curves in Fig. 8. Generally, the Rytov method explains the velocity shift of the FD simulations; the velocity shift increases with increasing travel distance, frequency and incident angle. However, there is a discrepancy between the values obtained from the Rytov method and those obtained from the FD simulations when the angle of incidence $\phi = \pi/2$ and the travel distance is short ($L < 400$ m).

5 DISCUSSION

5.1 The discrepancy between the Rytov method and FD simulations

The following two factors may be the main reasons for the discrepancy at short travel distances ($L < 400$ m) for the angle $\phi = \pi/2$ in Fig. 8. One is the assumption of long travel distances ($L \gg a_r$) in the calculation of eq. (29). The travel distance $L < 400$ m may not be long enough with respect to the correlation distance $a_r = 80$ m. The other is the use of the parabolic equation (see eq. 16) which neglects large-angle scattering. Employing the single scattering model (e.g. Sato 1977, 1982), we shall consider the 'isochronal scattering shell' which contributes to the energy around the direct wave. As the hypocentral distance increases, the shell is constrained to a neighbourhood around the line between the source and the receiver. As the shell is constrained to this region, small-angle scattering dominates large-angle scattering, resulting in a greater contribution of small-angle scattering with increasing hypocentral distance. On the contrary, when the hypocentral distance is short, the contribution from large-angle scattering is relatively large. Therefore, for short travel distances, the parabolic equation is probably not a good approximation for the wave equation.

5.2 Anisotropy of the effective average velocity

Fig. 9 shows the velocity shift versus the incident angle for the dominant frequencies $f_c = 40$, 80 and 120 Hz in the anisotropic random media with $a_x = 80$ m and $a_z = 40$ m. Solid curves represent values calculated with the Rytov method, and stars and circles are from the FD simulations. The result of the FD simulations for $f_c = 120$ Hz is not plotted because there is significant grid dispersion. The velocity shift increases with the incident angle; waves propagate faster in the direction of the long correlation distance. The ray theory may help to interpret this result; waves propagating in the direction of the long correlation distance can easily take long paths in the high-velocity portion whereas waves in the direction of the short correlation distance can only take short paths. We may imagine head waves in layered structures as an extreme case of this phenomenon. It should be noted that the ray theory predicts frequency independent behaviour in seismic wave propagation. However, Fig. 9 shows that the anisotropy in the velocity shift depends on the wave frequency; the anisotropy is more remarkable with increasing frequency.

P-wave velocity anisotropy observed in past studies has usually been interpreted in terms of the preferred orientations of cracks and minerals (e.g. Ishise & Oda 2005). Fig. 9 suggests that anisotropic random media could provide an alternative explanation. We note that Avendonk & Snieder (1994) and Samuelides & Mukerji (1998) also obtained similar results. However, those papers predicted frequency

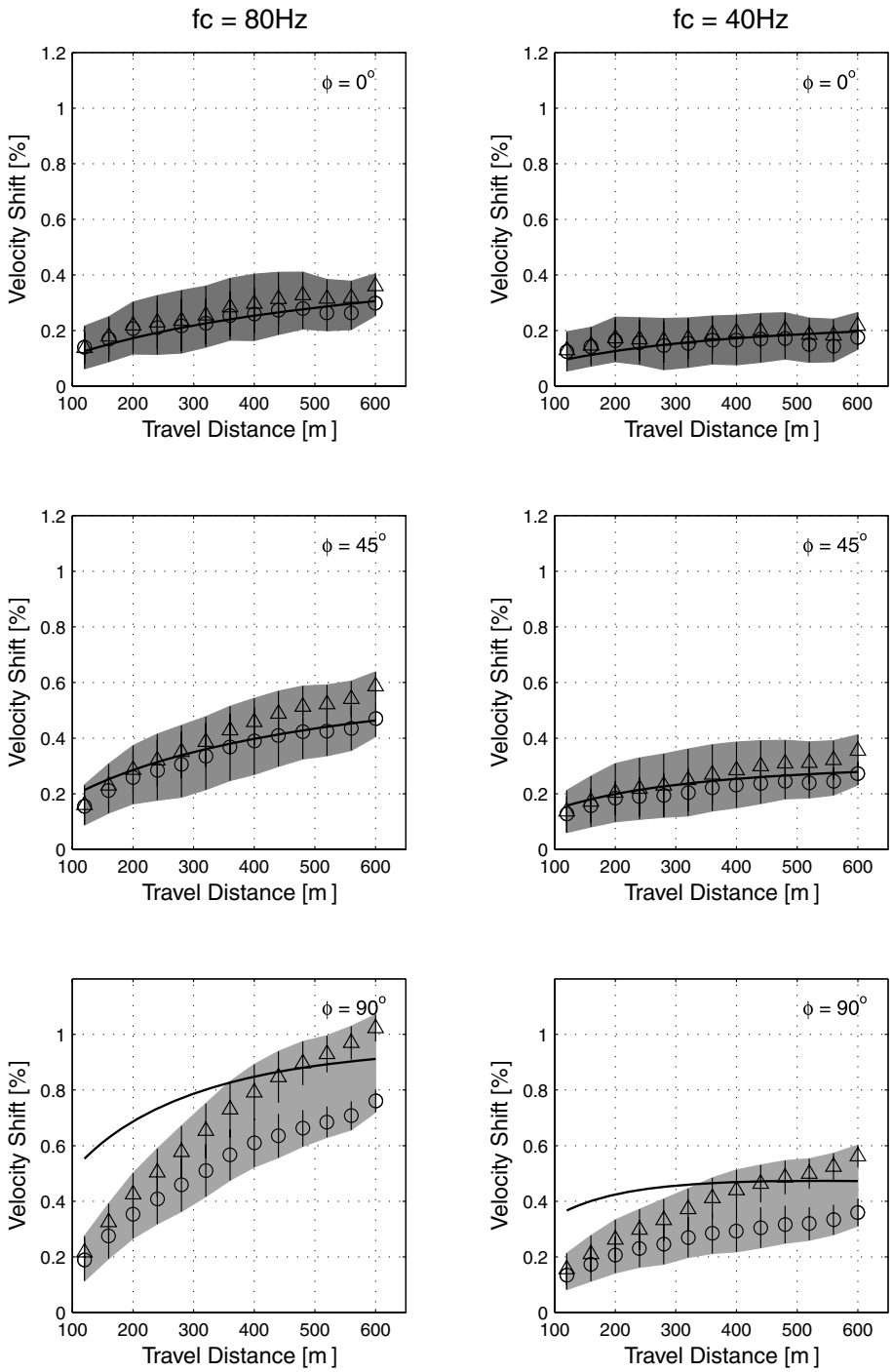

Figure 8. Velocity shift versus travel distances in anisotropic random media characterized by an exponential ACF with $\varepsilon = 0.05$, $a_x = 80$ m, $a_z = 40$ m and $V_0 = 2700$ m s^{-1} for angles of incidence $\phi = 0$, $\pi/4$ and $\pi/2$. Dominant frequencies are 80 Hz (left column) and 40 Hz (right column). Solid curves are plotted with values calculated using the Rytov method and the shaded areas are estimated from FD simulations. Triangles and circles are calculated from the velocity shift with t_1 and t_2 onsets, respectively. Error bars are estimated with a bootstrap method.

independent velocity anisotropy since they used the ray equation or the eikonal equation. On the other hand, the Rytov method can explain the frequency dependent velocity anisotropy since this method takes wave scattering into consideration (see Figs 8 and 9).

If we consider wave scattering to be due to randomly distributed aligned cracks instead of to the anisotropic random media, then we would also expect the velocity shift to exhibit frequency dependent anisotropy (see Fig. 6a, Kawahara & Yamashita, 1992; Fig. 4, Kawahara 1992). However, the velocity anisotropy caused by aligned cracks is more remarkable with decreasing frequency, contrary to the case of the anisotropic random media. This suggests that the tendency of the frequency dependence velocity anisotropy would be a good tool to discriminate between anisotropic random media and aligned cracks as an interpretation of observed velocity anisotropy. If we consider only

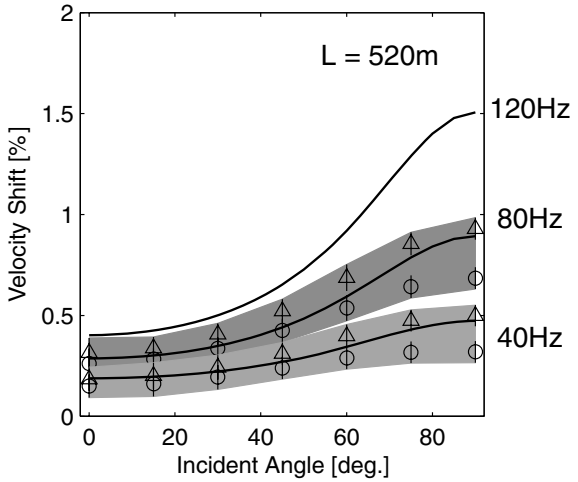

Figure 9. Velocity shift versus the angle of incidence in anisotropic random media characterized by an exponential ACF with $\varepsilon = 0.05, a_x = 80, a_z = 40$ m and $V_0 = 2700$ m s^{-1} at a travel distance of $L = 520$ m for the frequencies 40, 80 and 120 Hz. Solid curves are calculated with the Rytov method and shaded areas are estimated from FD simulations. Triangles and circles are calculated from the velocity shift with t_1 and t_2 onsets, respectively. Error bars are estimated with a bootstrap method.

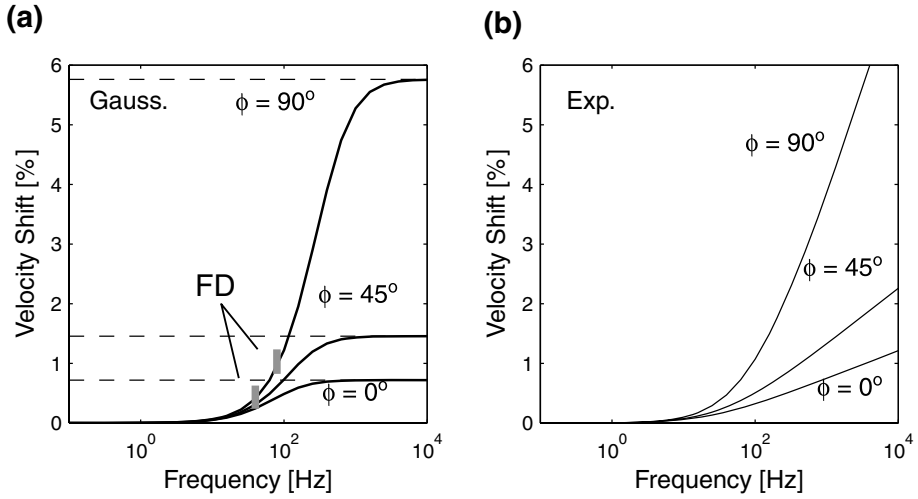

Figure 10. Velocity shift versus frequency calculated with the Rytov method (solid curves) at travel distance $L = 520$ m for angles of incidence 0, $\pi/4$ and $\pi/2$. (a) Random media characterized by a Gaussian ACF with $\varepsilon = 0.05, a_x = 80, a_z = 40$ m. Dashed lines indicate the high-frequency limit given by eq. (34). Grey bars indicate the velocity shift for the angle of incidence $\phi = \pi/2$ estimated from the FD simulations. (b) Random media characterized by an exponential ACF with $\varepsilon = 0.05$, $a_x = 80$ and $a_z = 40$ m.

the preferred orientation of minerals, or only the anisotropy of the elastic tensor, there would be no anisotropy in the excitation of later phases. On the other hand, the anisotropy of the later phases, or envelope shape, is one of the prominent features of anisotropic random media (Saito 2006). The above considerations indicate the importance of analysing not only velocity anisotropy but also its frequency dependence and the envelope shape to determine the dominant factor causing observed *P*-wave anisotropy.

5.3 Frequency dependence of the effective average velocity for the Gaussian ACF and the von Kármán type ACF

Fig. 10(a) shows the frequency dependence of the velocity shift in the anisotropic random media of the Gaussian ACF. The velocity shift at the low-frequency limit is zero; the effective average velocity is the same as the spatial average velocity. It should be noted that the Rytov method may not be valid at low frequency $ak < 1$, since the method uses high-frequency approximation, $ak \gg 1$. However, a velocity shift of zero at the low-frequency limit seems to be quite reasonable. The velocity shift increases with frequency and converges to constant values at the high-frequency limit. The values at the high-frequency limit of the velocity shift are given by eq. (34), and they are denoted by dashed lines in Fig. 10(a). The high-frequency limit theories, such as the eikonal equation or the ray equation, are expected to predict those values irrespective of the frequency. For example, the shift in the high-frequency limit is about 6 per cent when the angle of incidence $\phi = \pi/2$. However, the values of the velocity shift obtained by the FD simulations are about or below 1 per cent (plotted by grey lines in Fig. 10a), which

are almost the same as the values calculated with the Rytov method. This indicates that the Rytov method is superior to the high-frequency limit theories.

In Fig. 10(b), we plot the velocity shift for the case of the exponential ACF. The velocity shift at the low-frequency limit is zero and increases with frequency as in the case of the Gaussian ACF. However, in the exponential ACF, the velocity shift increases monotonically and does not converge at the high-frequency limit. Such a phenomenon was also predicted for isotropic random media (Shapiro *et al.* 1996; Baig & Dahlen 2004). This divergence of the velocity shift is due to the small-scale inhomogeneity; waves in random media characterized by an exponential ACF have substantial spectral amplitude in short wavelength components compared to waves in random media characterized by a Gaussian ACF. Hence, higher-frequency waves can take small high-velocity portions more efficiently in the case of the exponential ACF. It should be noted that the scattering attenuation of the initial wave is more dominant as the frequency increases (e.g. Shapiro & Kneib 1993). As a result, the selection of initial waves is more difficult as the frequency increases. In practice, the upper limit of the velocity shift for the case of the exponential ACF would be limited by the scattering attenuation before the divergence. The scattering attenuation in anisotropic random media is also an important research topic (e.g. Müller & Shapiro 2003, 2004; Hong & Wu 2005).

6 CONCLUSION

This study formulated the velocity shift in 2-D anisotropic random media with the Rytov method. We also showed that two different methods proposed by Samuelides (1998) and Shapiro *et al.* (1996) give the same resultant equation when we use some approximations. The velocity shift is represented by the PSDF of the random media. An analytic solution was obtained for the case of the Gaussian ACF. We numerically simulated the wave propagation using Ricker wavelets with dominant frequencies of 80 and 40 Hz. The random media were realized with a 2700 m s^{-1} spatial average velocity and the exponential ACF with 5 per cent rms fractional velocity fluctuation, 80 m correlation distance along the x-axis and 40 m along the z-axis. Numerical simulations showed that the wave propagates faster with increasing travel distance, frequency and the angle of incidence measured from the z-axis to the global ray direction: for the 80 Hz Ricker wavelet at a distance of 520 m, the values of the velocity shift are about 0.9 and 0.3 per cent in the directions along the x-axis and the z-axis, respectively. The Rytov method quantitatively explains the above tendencies of the velocity shift in general except for short travel distances along the x-axis. The discrepancy at short travel distances is probably due to the small angle scattering approximation and the long travel distance approximation in the Rytov method. The Rytov method can explain the frequency dependence of the velocity shift, whereas the high-frequency limit theories, such as eikonal and ray equations, cannot. Observations of P-wave velocity anisotropy have usually been interpreted in terms of preferred orientations of cracks and minerals in past studies. However this study indicates that wave scattering due to anisotropic random media can provide an alternative explanation for those observations. To identify the dominant factor causing the observed velocity anisotropy, it is important to analyse the frequency dependence of the anisotropy and the anisotropy of the later phase excitations in addition to the velocity anisotropy.

ACKNOWLEDGMENTS

The author wishes to thank O. Nishizawa and H. Sato for their discussion and comments, which greatly improved this manuscript. The author also thanks M. Korn, S. Shapiro and an anonymous reviewer for their helpful comments to the manuscript. This study was supported by JSPS and the Earthquake Research Institute cooperative research program.

REFERENCES

Aki, K., 1973. Scattering of *P* waves under the Montana LASA, *J. geophys. Res.,* **78,** 1334–1346.

Aki, K. & Chouet, B., 1975. Origin of coda waves: source, attenuation and scattering effects, *J. geophys. Res.,* **80,** 3322–3342.

Avendonk, H. & Snieder, R., 1994. A new mechanism for shape induced seismic anisotropy, *Wave Motion,* **20,** 89–98.

Baig, A.M. & Dahlen, F.A., 2004. Traveltime biases in random media and the S-wave discrepancy, *Geophys. J. Int.,* **158,** 922–938.

Chernov, L.A., 1960. *Wave Propagation in a Random Medium*, Mc-Graw Hill, New York.

Fehler, M., Sato, H. & Huang, L.-J., 2000. Envelope broadening of outgoing waves in 2-D random media: A comparison between the Markov approximation and numerical simulations, *Bull. seism. Soc. Am.,* **90,** 914–928.

Fehler, M. & Sato, H., 2003. Coda, *Pure appl. Geophys.,* **160,** 541–554.

Flatté, S.M. & Wu, R.S., 1988. Small-scale structure in the lithosphere and asthenosphere deduced from arrival time and amplitude fluctuation at NORSAR, *J. geophys. Res.,* **93,** 6601–6614.

Hong, T.-K. & Wu, R.S., 2005. Scattering of elastic waves in geometrically anisotropic random media and its implication to sounding of heterogeneity in the Earth's deep interior, *Geophys. J. Int.,* **163,** 324–338.

Ishimaru, A., 1978. *Wave Propagation and Scattering in Random Media*, Academic Press, New York.

Ishise, M. & Oda, H., 2005. Three-dimensional structure of *P*-wave anisotropy beneath the Tohoku district, northeast Japan, *J. geophys. Res.,* **110,** B07304, doi:10.1029/2004JB003599.

Iooss, B., 1998. Seismic reflection traveltimes in two-dimensional statistically anisotropic random media, *Geophys. J. Int.,* **135,** 999–1010.

Kawahara, J., 1992. Scattering of P, SV waves by random distribution of aligned open cracks, *J. Phys. Earth.,* **40,** 517–524.

Kawahara, J. & Yamashita, T., 1992. Scattering of elastic waves by a fracture zone containing randomly distributed cracks, *Pure appl. Geophys.,* **139,** 121–144.

Korn, M. & Sato, H., 2005. Synthesis of plane vector wave envelopes in two-dimensional random elastic media based on the Markov approximation and comparison with finite-difference simulations, *Geophys. J. Int.,* **161,** 839–848.

Kravtsov, Y.A., Müller, T.M., Shapiro, S.A. & Buske, S., 2003. Statistical properties of reflection traveltimes in 3-D randomly inhomogeneous and anisomeric media, *Geophys. J. Int.,* **154,** 841–851.

Mukerji, T., Mavko, G., Mujica, D. & Lucet, N., 1995, Scale-dependent seismic velocity in heterogeneous media, *Geophysics,* **60,** 1222–1233.

Müller, G., Roth, M. & Korn, M., 1992, Seismic-wave traveltimes in random media, *Geophys. J. Int.,* **110,** 29–41.
Müller, T.M. & Shapiro, S.A., 2003. Amplitude fluctuations due to diffraction and refraction in anisotropic random media: implications for seismic scattering attenuation estimates, *Geophys. J. Int.,* **155,** 139–148.
Müller, T.M. & Shapiro, S.A., 2004, Scattering attenuation in randomly layered structures with finite lateral extent: a hybrid *Q* model, *Geophysics,* **69,** 1530–1534.
Petersen, N.V., 1990. Inverse kinematic problem for a random gradient medium in geometric optics approximation, *Pure appl. Geophys.,* **132,** 417–437.
Roth, M., Müller, G. & Snieder, R., 1993. Velocity shift in random media, *Geophys. J. Int.,* **115,** 552–563.
Rytov, S.M., Kravtsov, Y.A. & Tatarskii, V.I., 1989. *Principles of Statistical Radio Physics (Vol. 4) Wave Propagation Through Random Media*, Springer-Verlag, Berlin.
Saito, T., 2006. Synthesis of scalar-wave envelopes in 2-D weakly anisotropic random media using the Markov approximation, *Geophys. J. Int.,* **165,** 501–515.
Saito, T., Sato, H. & Ohtake, M., 2002. Envelope broadening of spherically outgoing waves in three-dimensional random media having power-law spectra, *J. geophys. Res.,* **107**(B5), 2089, doi:10.1029/2001JB000264.
Saito, T., Sato, H., Ohtake, M. & Obara, K., 2005. Unified explanation of envelope broadening and maximum-amplitude decay of high-frequency seismograms based on the envelope simulation using the Markov approximation: forearc side of the volcanic front in northeastern Honshu, Japan, *J. geophys. Res.,* **110,** B01304, doi:10.1029/2004JB003225.
Samuelides, Y., 1998. Velocity shift using the Rytov approximation, *J. acoust. Soc. Am.,* **104,** 2596–2603.
Samuelides, Y. & Mukerji, T., 1998. Velocity shift in heterogeneous media with anisotropic spatial correlation, *Geophys. J. Int.,* **134,** 778–786.
Sato, H., 1977. Energy propagation including scattering effect: single isotropic scattering approximation, *J. Phys. Earth,* **25,** 27–41.
Sato, H., 1982. Coda wave excitation due to nonisotropic scattering and nonspherical source radiation, *J. geophys. Res.,* **87,** 8665–8674.
Sato, H., 1989. Broadening of seismogram envelopes in the randomly inhomogeneous lithosphere based on the parabolic approximation: southeastern Honshu, Japan, *J. geophys. Res.,* **94,** 17 735–17 747.
Sato, H. & Fehler, M., 1998. *Seismic Wave Propagation and Scattering in the Heterogeneous Earth*, Springer-Verlag, New York.
Shapiro, S.A. & Kneib, G., 1993. Seismic attenuation by scattering: theory and numerical results, *Geophys. J. Int.,* **114,** 373–391.
Shapiro, S.A., Schwarz, R. & Gold, N., 1996. The effect of random isotropic inhomogeneities on the phase velocity of seismic waves, *Geophys. J. Int.,* **127,** 783–794.
Sivaji, C., Nishizawa, O. & Fukushima, Y., 2001. Relationship between fluctuations of arrival time and energy of seismic waves and scale length of heterogeneity: an inference from experimental study, *Bull. seism. Soc. Am.,* **91,** 292–303.
Sivaji, C., Nishizawa, O., Kitagawa, G. & Fukushima, Y., 2002. A physical-model study of the statistics of seismic waveform fluctuations in random heterogeneous media, *Geophys. J. Int.,* **148,** 575–595.
Spetzler, J., Sivaji, C., Nishizawa, O. & Fukushima, Y., 2002. Scattering theory based on a laboratory experiment using ultrasonic waves and numerical simulations by finite-difference method, *Geophys. J. Int.,* **148,** 165–178.
Wielandt, E., 1987. On the validity of the ray approximation for interpreting delay times, in *Seismic Tomography*, pp. 85–98, ed. Nolet, G., Reidel, Dordrecht.
Wu, R.S., Xu, Z. & Li X.-P., 1994. Heterogeneity spectrum and scale anisotropy in the upper crust revealed by the German continental deep-drilling (KTB) holes, *Geophys. Res. Lett.,* **21,** 911–914.

APPENDIX A: DERIVATION OF EQ. (25)

In this appendix, we briefly explain the derivation of eq. (25).

Taking the Fourier transform with respect to $r_\perp$, we write eq. (21) as

$$2ik\frac{\partial \hat{\Xi}_2(k_\perp, r)}{\partial r} - {k_\perp}^2 \hat{\Xi}_2(k_\perp, r) + \hat{F}(k_\perp, r) = 0, \tag{A1}$$

where

$$\hat{\Xi}_2(k_\perp, r) = \int_{-\infty}^{\infty} \Xi_2(r_\perp, r) \exp(-ik_\perp r_\perp)\, dr_\perp, \tag{A2}$$

and

$$\hat{F}(k_\perp, r) = \int_{-\infty}^{\infty} \left(\frac{\partial \Xi_1(r_\perp, r)}{\partial r_\perp}\right)^2 \exp(-ik_\perp r_\perp)\, dr_\perp. \tag{A3}$$

Taking the ensemble average of the solution of eq. (A1), we obtain

$$\langle \hat{\Xi}_2(k_\perp, r)\rangle = \frac{i}{2k}\int_0^r \exp\left\{-i\frac{{k_\perp}^2(r-r')}{2k}\right\} \langle \hat{F}(k_\perp, r')\rangle\, dr'. \tag{A4}$$

Substituting eq. (23) into eq. (A3), we calculate the ensemble average of $\hat{F}(k_\perp, r')$ as

$$\begin{aligned}\langle \hat{F}(k_\perp, r)\rangle = {} & \frac{k^2}{2\varepsilon^2\pi}\int_0^r dr' \int_0^r dr'' \int_{-\infty}^{\infty} dk'_\perp \int_{-\infty}^{\infty} dk''_\perp \delta(k_\perp - k'_\perp - k''_\perp) k'_\perp k''_\perp \\ & \times \exp\left\{-i\frac{({k'_\perp}^2 + {k''_\perp}^2)r}{2k}\right\} \exp\left\{-i\frac{{k'_\perp}^2 r' + {k''_\perp}^2 r''}{2k}\right\} \langle \hat{\xi}(k'_\perp, r')\hat{\xi}(k''_\perp, r'')\rangle,\end{aligned} \tag{A5}$$

where $\hat{\xi}(k_\perp, r)$ is defined in eq. (24). The ensemble average quantity appearing in the right-hand side of (A5) can be written as

$$\langle \hat{\xi}(k'_\perp, r')\hat{\xi}(k''_\perp, r'')\rangle = 2\pi\delta(k'_\perp + k''_\perp)\int_{-\infty}^{\infty} dr_{\perp d} \exp\left\{-i\frac{(k'_\perp - k''_\perp)r_{\perp d}}{2}\right\} R(r_{\perp d}, r' - r''), \tag{A6}$$

where R is the ACF in $(r_\perp, r)$ coordinates. Substituting eqs (A5) and (A6) into (A4), and taking the inverse Fourier transform, we obtain

$$\begin{aligned}\langle \Xi_2(r_\perp, L)\rangle &= \frac{1}{2\pi}\int_{-\infty}^{\infty}\langle \hat{\Xi}_2(k_\perp, L)\rangle \exp(ik_\perp r_\perp)dk_\perp \\ &= -\frac{ik}{4\pi\varepsilon^2}\int_0^L dr\int_0^r dr'\int_0^r dr''\int_{-\infty}^{\infty} dk'_\perp {k'_\perp}^2 \exp\left\{-\frac{i{k'_\perp}^2(2r-r'-r'')}{2k}\right\} \\ &\quad\times\int_{-\infty}^{\infty} dr_{\perp d}\, R(r_{\perp d}, r'-r'')\exp\left(-ik'_\perp r_{\perp d}\right). \end{aligned} \tag{A7}$$

APPENDIX B: DERIVATION BASED ON SHAPIRO *ET AL.* (1996)

In this appendix, we formulate the velocity shift in the 2-D anisotropic random media based on Shapiro *et al.* (1996).

The wavefield $\Xi(r_\perp, r)$ defined by eq. (19) is decomposed into real and imaginary parts as $\Xi(r_\perp, r) = \chi(r_\perp, r) + i\varphi(r_\perp, r)$, where the real part χ is the log-amplitude fluctuation and the imaginary part φ is the phase fluctuation. Shapiro *et al.* (1996) derived a relation among the ensemble average of the phase fluctuation $\langle\varphi\rangle$, the phase of the ensemble average wavefield φ_c, the phase of the wavefield in a homogeneous medium φ_0, and the cross-variance of the log-amplitude fluctuation and the phase fluctuation $\sigma^2_{\chi\varphi}$; namely that $\langle\varphi\rangle \approx \varphi_c - \varphi_0 - \sigma^2_{\chi\varphi}$ holds, where $\sigma^2_{\chi\varphi}$ is defined by $\sigma^2_{\chi\varphi} \equiv \langle\chi - \langle\chi\rangle\rangle\langle\varphi - \langle\varphi\rangle\rangle \approx \langle\chi\varphi\rangle$. When we use the parabolic equation, the phase φ_c of the ensemble average wavefield is the same as the phase of a wavefield φ_0 in a homogeneous medium (p. 243, Sato & Fehler 1998). Then, the velocity shift given by eq. (18) is represented as

$$\frac{\delta V}{V_0} \approx \frac{\sigma^2_{\chi\varphi}}{kL} \approx \frac{\langle\chi\varphi\rangle}{kL}. \tag{B1}$$

We briefly show the derivation of $\sigma^2_{\chi\varphi}$ in the following. Substituting $\hat{u}(\boldsymbol{x}) = \hat{u_0}(\boldsymbol{x})\exp\{\Xi(\boldsymbol{x})\}$ into the wave equation eq. (15), we obtain

$$\Xi(\boldsymbol{x}) = \frac{1}{\hat{u_0}(\boldsymbol{x})}\int_{-\infty}^{\infty}\int_{-\infty}^{\infty} G_0(\boldsymbol{x}-\boldsymbol{x}')\left\{2\xi(\boldsymbol{x}')k^2 - \nabla\Xi(\boldsymbol{x}')\cdot\nabla\Xi(\boldsymbol{x}')\right\}\hat{u}_0(\boldsymbol{x}')d\boldsymbol{x}', \tag{B2}$$

where $\hat{u}_0(\boldsymbol{x}) = \exp(ikr)$ and ∇' is the gradient with respect to $\boldsymbol{x}'$. The Green's function G_0 satisfies $\triangle G_0(\boldsymbol{x}) + k^2 G_0(\boldsymbol{x}) = \delta(\boldsymbol{x})$. By iteration, we can obtain a series solution of eq. (B2). As a first iteration, we let $\Xi(\boldsymbol{x}') = 0$ inside the integral in eq. (B2). When small-angle scattering around the forward direction dominates large-angle scattering, we may consider the range $r \gg r_\perp$ in the $(r_\perp, r)$ coordinates (Fig. 2) and approximate G_0 as

$$G_0(\boldsymbol{x}) \approx \begin{cases} \dfrac{-i}{4}\sqrt{\dfrac{2}{\pi kr}}\exp\left\{ik\left(r + \dfrac{{r_\perp}^2}{2r}\right) - \dfrac{i\pi}{4}\right\} & r > 0 \\ 0 & r \le 0. \end{cases} \tag{B3}$$

Substituting eq. (B3) into the first iteration solution, we obtain

$$\Xi(r_\perp, L) = \frac{-ik}{2\pi}\int_0^L dr'\int_{-\infty}^{\infty} dk_\perp \exp(ik_\perp r_\perp)\exp\left\{\frac{-ik_\perp{}^2(L-r')}{2k}\right\}\hat{\xi}(k_\perp, r'), \tag{B4}$$

where $\hat{\xi}$ is defined in eq. (24). From eq. (B4) and its complex conjugate, we obtain

$$\begin{aligned}\chi(r_\perp, L) &= \frac{-k}{2\pi}\int_0^L dr'\int_{-\infty}^{\infty} dk_\perp \exp(ik_\perp r_\perp)\sin\left\{\frac{k_\perp{}^2(L-r')}{2k}\right\}\hat{\xi}(k_\perp, r') \\ \varphi(r_\perp, L) &= \frac{-k}{2\pi}\int_0^L dr'\int_{-\infty}^{\infty} dk_\perp \exp(ik_\perp r_\perp)\cos\left\{\frac{k_\perp{}^2(L-r')}{2k}\right\}\hat{\xi}(k_\perp, r'). \end{aligned} \tag{B5}$$

For two points $(r_{\perp 1}, L)$ and $(r_{\perp 2}, L)$ at travel distance L, we obtain the following:

$$\begin{aligned}\langle\chi(r_{\perp 1}, L)\varphi(r_{\perp 2}, L)\rangle &= \frac{k^2}{(2\pi)^2}\int_0^L dr'\int_0^L dr''\int_{-\infty}^{\infty} dk'_\perp\int_{-\infty}^{\infty} dk''_\perp \exp(ik'_\perp r_{\perp 1} + ik''_\perp r_{\perp 2}) \\ &\quad\times\sin\left\{\frac{{k'_\perp}^2(L-r')}{2k}\right\}\cos\left\{\frac{{k''_\perp}^2(L-r'')}{2k}\right\}\langle\hat{\xi}(k'_\perp, r')\hat{\xi}(k''_\perp, r'')\rangle. \end{aligned} \tag{B6}$$

Substituting eq. (A6) into eq. (B6) and introducing centre of mass and difference coordinates, $r_c = (r' + r'')/2$ and $r_d = r' - r''$, we can evaluate eq. (B6) as follows:

$$\begin{aligned}
\langle \chi(r_{\perp 1}, L)\varphi(r_{\perp 2}, L)\rangle &= \frac{k^2}{4\pi}\int_{-L}^{L} dr_d \int_{|r_d|}^{L-|r_d|/2} dr_c \int_{-\infty}^{\infty} dk_\perp \exp\{ik_\perp(r_{\perp 1} - r_{\perp 2})\}\left\{\sin\frac{{k_\perp}^2(L-r_c)}{k} - \sin\frac{{k_\perp}^2 r_d}{k}\right\} \\
&\quad \times \int_{-\infty}^{\infty} dr_{\perp d} \exp(-ik_\perp r_{\perp d}) R(r_{\perp d}, r_d) \\
&\approx \frac{k^3}{2\pi}\int_{-L}^{L} dr_d \int_{-\infty}^{\infty} dk_\perp \frac{1}{{k_\perp}^2}\exp\{ik_\perp(r_{\perp 1} - r_{\perp 2})\}\sin\frac{{k_\perp}^2 L}{2k}\sin\frac{{k_\perp}^2(L-|r_d|)}{2k} \\
&\quad \times \int_{-\infty}^{\infty} dr_{\perp d} \exp(-ik_\perp r_{\perp d}) R(r_{\perp d}, r_d) \\
&\approx \frac{k^3}{2\pi}\int_{-\infty}^{\infty} dr_d \int_{-\infty}^{\infty} dk_\perp \frac{1}{{k_\perp}^2}\exp\{ik_\perp(r_{\perp 1} - r_{\perp 2})\}\sin^2\frac{{k_\perp}^2 L}{2k} \\
&\quad \times \int_{-\infty}^{\infty} dr_{\perp d} \exp(-ik_\perp r_{\perp d}) R(r_{\perp d}, r_d) \\
&= \frac{k^3}{\pi}\int_{-\infty}^{\infty} dk_\perp \frac{1}{{k_\perp}^2}\exp\{ik_\perp(r_{\perp 1} - r_{\perp 2})\}\sin^2\left\{\frac{{k_\perp}^2 L}{2k}\right\} P(k_\perp, 0) \\
&= \frac{\varepsilon^2 k^3 a_t a_r}{\pi}\int_{-\infty}^{\infty} dk_\perp \frac{1}{{k_\perp}^2}\exp\{ik_\perp(r_{\perp 1} - r_{\perp 2})\}\sin^2\left\{\frac{{k_\perp}^2 L}{2k}\right\}\bar{P}(a_\perp k_\perp),
\end{aligned} \tag{B7}$$

where effective correlation distances a_t and a_r are given by eq. (32). During this calculation, we considered the contribution from $R(r_{\perp d}, r_d)$ to be large at $r_d < a$ when $L > a$. Also, we supposed that $R(r_{\perp d}, r_d) \approx R(r_{\perp d}, -r_d)$ by observing that the contribution of $R(r_{\perp d}, r_d)$ becomes larger as $|r_{\perp d}|$ becomes smaller. Setting $r_{\perp 1} = r_{\perp 2}$, we obtain $\sigma^2_{\chi\varphi}$. Substituting the resultant equation into eq. (B2), we finally obtain the velocity shift as

$$\frac{\delta V}{V_0} \approx \frac{\varepsilon^2 k^2 a_\perp a_r}{\pi L}\int_0^{\infty} dk_\perp \frac{1}{{k_\perp}^2}\sin^2\left\{\frac{{k_\perp}^2 L}{2k}\right\}\bar{P}(a_\perp k_\perp). \tag{B8}$$

This is the same as eq. (31).